



1 **Bare-earth DEM Generation from ArcticDEM, and Its Use in** 2 **Flood Simulation**

3 **Yinxue Liu^{1*}, Paul D Bates¹, Jeffery C Neal¹**

4 ^{1†} School of Geographical Sciences, University of Bristol, Bristol, UK

5 *Correspondence to:* Yinxue Liu (Yinxue.liu@bristol.ac.uk)

6 **Abstract**

7 In urban areas, topography data without above ground objects are typically preferred in
8 wide-area flood simulation, but are not yet available for many locations globally. High-
9 resolution satellite photogrammetry DEMs, like ArcticDEM, are now emerging and could
10 prove extremely useful for global urban flood modelling, however approaches to generate bare-
11 earth DEMs from them have not yet been fully investigated. In this paper, we test the use of
12 two morphological filters (Simple Morphological Filter-SMRF and Progressive Morphological
13 Filter-PMF) to remove surface artefacts from ArcticDEM using the city of Helsinki (192 km²)
14 as a case study. The optimal filter is selected and used to generate a bare-earth version of
15 ArcticDEM. Using a LIDAR DTM as a benchmark, the elevation error and flooding simulation
16 performance for a pluvial event were then evaluated at 2 m and 10 m spatial resolution,
17 respectively. The SMRF was found to be more effective at removing artefacts than PMF over
18 a broad parameter range. For the optimal ArcticDEM-SMRF the elevation RMSE was reduced
19 by up to 70% over the uncorrected DEM, achieving a final value of 1.02 m. The simulated
20 water depth error was reduced to 0.3 m, which is comparable to typical model errors using
21 LIDAR DTM data. This paper indicates that the SMRF can be directly applied to generate a
22 bare-earth version of ArcticDEM in urban environments, although caution should be exercised
23 for areas with densely packed buildings or vegetation. The results imply that where LIDAR
24 DTMs do not exist, widely available high-resolution satellite photogrammetry DEMs could be
25 used instead.

26 **1 Introduction**

27 The availability of an accurate bare-earth Digital Elevation Model (DEM) is important
28 to many research fields, including identifying drainage related features and modelling flood
29 inundation (Garbrecht and Martz, 2000; Yamazaki et al., 2014), deriving topography indices
30 such as slope, orientation, and rugosity (Moudrý et al., 2018), estimating forest biomass and
31 carbon (Jensen et al., 2016), and constructing 3D building heights (Marconcini et al., 2014).



32 For wide-area flood simulation in urban areas, a bare-earth DEM (i.e., a terrain model without
33 surface artefacts) is preferable in most circumstances to a Digital Surface Model (DSM) which
34 includes them. This is because the decision to include above terrain artefacts or not is a
35 consequence of the selected simulation resolution. Only when the simulation is conducted at
36 grid sizes allowing the resolution of building shapes and the street layout (typically < 5 m in
37 most urban topologies worldwide) does a DSM become useful. When aggregated to coarser
38 resolutions, the height of the surface artefacts contained in the DSM can block or alter flow
39 pathways in ways that lead to anomalous results when these data are used in hydrodynamic
40 modelling (Neal et al., 2009). Inundation simulations over regional and national scales usually
41 only become feasible with non-building resolving grid resolutions because of the exponentially
42 increased computational cost of running fine grid models and the limited availability of national
43 DEMs with resolutions finer than 5 m. Even at city and sub-city scales, non-building resolving
44 models may be preferable for ensemble and event set simulations (Mason et al., 2007; Schubert
45 and Sanders, 2012). As a result, bare-earth DEMs (also known as Digital Terrain Models or
46 DTMs) are essential for flood inundation simulations in urban areas and can also be beneficial
47 to a broad range of other research fields.

48 Unlike traditional, ground-based field survey, modern wide-area DEM collection
49 techniques rely on remote sensing from ground vehicle, airborne and satellite platforms. All
50 DEMs derived in this way include the heights of built-up area artefacts and vegetation to some
51 extent and require significant post-processing to obtain a bare-earth DEM. Commonly used
52 DEMs are collected using techniques including Interferometric Synthetic Aperture Radar (i.e.,
53 InSAR), optical stereo mapping and LIDAR. These different techniques, combined with the
54 platforms and the specific instrument characteristics, offer DEMs with varied coverage,
55 resolution, and accuracy (Lakshmi and Yarrakula, 2018; Zaidi et al., 2018). For example,
56 spaceborne and globally available InSAR DEMs offer wide coverage but they are constrained
57 by the geometry of the interferometric baseline and the temporal sampling of the spaceborne
58 platform and InSAR technique. The derived DEMs therefore have limited horizontal resolution
59 and accuracy (SRTM at ~30 m spatial resolution has reported mean absolute vertical error of
60 6 m, TanDEM-X at ~12 m spatial resolution has 90% linear error (i.e., LE90) in the vertical of
61 around 2 m) (Rodriguez et al., 2006; Wessel et al., 2018). Such vertical errors are significant
62 compared to the amplitude of most river flood waves, which typically range from 1-2 m up to
63 ~12 m for the Amazon River at Manaus in Brazil (Trigg et al., 2009; Bates et al., 2013). Whilst
64 global InSAR DEM errors can be reduced by intelligent processing (O'Loughlin et al., 2016;



65 Yamazaki et al, 2017; Archer et al., 2018; Liu et al., 2021; Hawker et al., 2022) and by
66 aggregating to coarser grid resolutions to mitigate random errors, they remain distinctly sub-
67 optimal for much flood inundation modelling (Schumann and Bates, 2018). Instead, inundation
68 modelling is best conducted with DEMs generated using airborne LIDARs for most
69 applications. These have high accuracy, with a typical vertical RMSE of 0.05–0.2 m (Faherty
70 et al., 2020), and spatial resolution of 1-2 m such that they can identify the detailed structure
71 of floodplain geomorphology, buildings, vegetation, and important linear features such as flood
72 defences and their crest elevations. However, due to their (relatively) high cost of collection,
73 freely available LIDAR data only cover ~0.005% of the global land surface (Hawker et al.,
74 2018). DEMs derived from high-resolution stereo images, such as WorldView, have the
75 potential to cover the land surface globally with spatial resolution (and also perhaps accuracy)
76 comparable to LIDAR (Noh and Howat, 2015; Hu et al., 2016; Shean et al., 2016; DeWitt et
77 al., 2017). Whilst stereo photogrammetry was previously used to develop the (now superseded)
78 publicly available ASTER DEM (Hirano et al., 2003), more recent DEMs derived from high-
79 resolution photogrammetry such as WorldView, GeoEye, IKONOS and Pleiades images have
80 been kept as commercial products with a cost that is prohibitive for most academic studies.
81 However, the recent public release of an unprecedented resolution (2 m) satellite photogrammetry
82 DEM, ArcticDEM (Porter et al., 2018, <https://www.pgc.umn.edu/data/arcticdem/>), has brought
83 opportunities to explore the potential of such a product in flood inundation modelling.
84 ArcticDEM covers areas above 60°N and was produced using the SETSM method from in-
85 track and cross-track high-resolution (~0.5 m) imagery acquired by the WorldView and
86 GeoEye satellites. Using similar stereo-photogrammetry techniques, Google is also developing
87 a very high-resolution DEM using multiple satellite sources (Ben-Haim et al., 2019). However,
88 both products are DSMs and therefore contain surface artefacts which need to be removed to
89 enable their use in a range of geophysics applications including wide-area flood inundation
90 modelling. Previous research efforts to generate bare-earth terrain data from previously
91 released global DEMs such as SRTM and TanDEM-X have relied heavily on auxiliary data to
92 remove artefacts. For these next generation of high-resolution photogrammetry DEMs,
93 auxiliary data at comparable resolution to the DEM does not yet exist and different approaches
94 must be proposed.

95 Considering the high resolution of these photogrammetry DEMs, the algorithms
96 already developed to create bare-earth DEMs from LIDAR are likely to be applicable to this
97 task. For example, DeWitt et al. (2017) have shown that applying LIDAR filtering procedures



98 to a WorldView-generated DEM in densely vegetated areas can remove vegetation artefacts
99 and achieve a bare-earth terrain representation with accuracy comparable to LIDAR. Numerous
100 research studies have been conducted in the past decade to generate bare-earth DEMs (i.e.,
101 DTMs) from LIDAR point clouds (Sithole and Vosselman, 2004; Chen et al., 2007; Meng et
102 al., 2009; Zhang et al., 2016). Filtering strategies were reviewed by Chen et al. (2017), and
103 morphology-based filters were reported as robust and capable of removing non-ground objects.
104 Notably, Zhang et al (2003) proposed a progressive morphological filter (PMF) for removing
105 non-ground measurements from airborne LIDAR. The PMF method has subsequently
106 advanced by enabling automatic extraction of ground points from LIDAR measurements with
107 minimal human interaction and is now widely used as a base filter to classify ground and non-
108 ground points (Cui et al., 2013; Hui et al., 2016; Tan et al., 2018). Evolved from the
109 morphological filter idea, Pingel et al (2013) developed the Simple Morphological Filter
110 (SMRF) by designating the window size increasement strategy of the filter and employing a
111 computationally inexpensive technique to interpolate the non-ground pixels. The SMRF was
112 reportedly able to achieve low misclassification errors (2.97%) among 11 filter algorithms for
113 LIDAR DEM samples with various configuration of slope and artefacts and to be robust to the
114 algorithm parameterization (Zhang et al., 2016). However, despite previous research applying
115 LIDAR filtering strategies to WorldView photogrammetric DEMs (Rokhmana and Sastra,
116 2020), none of these filters has been tested on ArcticDEM and research about the performance
117 of different filters for removing surface artefacts from high-resolution photogrammetric DSMs
118 is also lacking, especially in urban areas.

119 Given their unprecedented resolution and potential wide-area coverage, bare-earth
120 photogrammetric DEMs can possibly be used to advance flood inundation simulation at
121 regional scales and beyond. Although at this stage the access to these DEMs is restricted, they
122 are very promising and could become an alternative to LIDAR data in the future as a result of
123 their much lower cost. This could especially benefit developing countries where wide coverage
124 of LIDAR data is likely to prove unaffordable for the foreseeable future. This research therefore
125 aims to develop an approach to generate bare-earth DEMs from ArcticDEM and to examine
126 the use of the data in flood inundation simulation. The proposed approach is expected to be
127 generally applicable to other high-resolution (~m scale) photogrammetry DEMs as well as
128 ArcticDEM. We first compare the ability of progressive and simple morphological filters (PMF
129 and SMRF) to generate a bare-earth DEM from ArcticDEM in the city of Helsinki, Finland by
130 evaluating the filtered ArcticDEMs against a reference bare-earth LIDAR data set. Next, for



131 the best performing filter a set of parameter combinations was applied to generate a realization
132 ensemble of filtered ArcticDEM, whose error metrics were then analyzed against the parameter
133 settings. We then use both the original ArcticDEM and filtered ArcticDEM realizations to
134 simulate a pluvial flooding scenario for Helsinki and compare these results to an identical
135 simulation using the LIDAR DTM. Pluvial flood simulation is a difficult for hydrodynamic
136 models even with excellent terrain data and therefore poses a rigorous and diagnostic test.
137 Lastly, limitations of the current research and future work that could further facilitate the use
138 of a bare-earth version of ArcticDEM in flood inundation simulation is discussed.

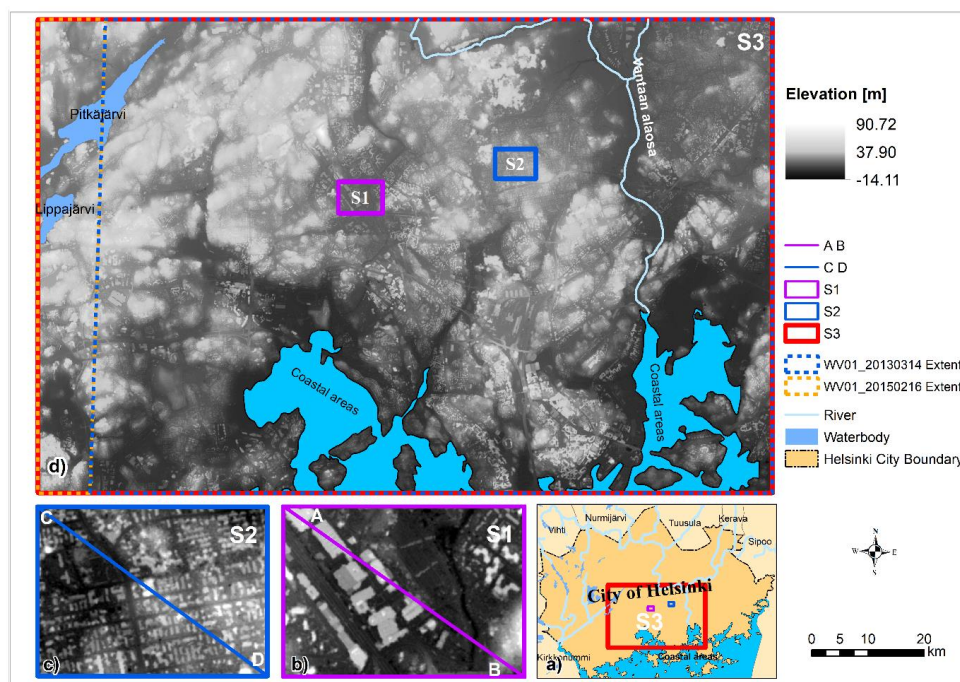
139 **2 Data source and study site**

140 ArcticDEM is stereo-photogrammetry DSM generated from in-track and cross-track
141 high-resolution (~0.5 m) imagery acquired by the DigitalGlobe constellation of optical imaging
142 satellites. The majority of ArcticDEM data was generated from the panchromatic bands of the
143 WorldView-1, WorldView-2, and WorldView-3 satellites. A small percentage of data was also
144 sourced from the GeoEye-1 satellite sensor. ArcticDEM is available in two formats: strip and
145 mosaic. Strip data is the output extracted by the TIN based Search-space Minimization
146 algorithm (Noh and Howat, 2015) and preserves the original source material temporal
147 resolution. Mosaic data is compiled from multiple strips that have been co-registered, blended,
148 and feathered to reduce edge-matching artifacts. Due to the errors in the sensor model, the
149 geolocation of the generated ArcticDEM has systematic offsets in the vertical and horizontal
150 directions which are reported in the product's meta-data. Offsets for the mosaic data are
151 unknown so therefore the strip data set with the original horizontal resolution at 2 m (version
152 3.0) was used as the baseline DEM in this paper. The offset values of each strip data were
153 applied before generating the bare-earth ArcticDEM.

154 The city of Helsinki was selected as a study site for the following reasons: 1) both
155 ArcticDEM and a high accuracy LIDAR DTM are available at this site, with the vertical error
156 of the LIDAR DTM reported as 0.3 m; and 2) it is a typical urban environment with sparse to
157 medium density buildings mixed with large patches of vegetation; 3) as the most populated city
158 above 60°N, the Helsinki metropolitan areas is very vulnerable to flooding. To standardize the
159 vertical reference system, the quasigeoid height was subtracted from ArcticDEM, converting
160 its reference system from WGS84 ellipsoid height to the Finland National Vertical Reference-
161 N2000 that is used for the LIDAR data. This conversion has an accuracy of 0.02 m.



162 Within the city of Helsinki two building-dominated samples (S1 and S2, both covering
163 areas of $\sim 0.7 \text{ km}^2$) were chosen to compare the effectiveness of two selected morphological
164 filters: the PMF and the SMRF. Sample 1 is characterized by buildings with floor areas up to
165 10000 m^2 , whereas smaller buildings (floor areas of $\sim 500 \text{ m}^2$) are distributed throughout
166 Sample 2. A larger third sample (S3, which includes both S1 and S2) was selected to conduct
167 the bare-earth DEM generation and to assess the filter's performance in a complex urban
168 environment. Flood inundation modelling of the resulting DEM data was also performed over
169 sample area S3 (Fig. 1). The ArcticDEM strips data derived from WorldView-1 images
170 acquired on the 14th of March 2013 (WV01_20130314) and on the 16th of February 2015
171 (WV01_20150216) were found to cover most areas of S3 (92% and 99%, respectively).
172 Considering the possible bias caused by forest and snow, the ArcticDEM strips with source
173 images acquired during leaf-off seasons and under snow-free conditions are preferable. The
174 Finish forests are reported to be mostly evergreen with $\sim 10\%$ of deciduous trees (Majasalmi
175 and Rautiainen, 2021). The source images of both strips were acquired during leaf-off
176 conditions. The snow situation on the image acquisition dates was analyzed using the MODIS
177 NDSI_Snow Cover data (Hall et al., 2016). The acquisition date of the strip WV01_20130314
178 was found to be much less covered by snow compared to that of the WV01_20150216 strip.
179 Therefore, the strip WV01_20130314 was used as the main data source and areas within S3
180 which this strip does not cover or where voids were present were filled with data from the strip
181 WV01_20150216. These mosaiced strip data are shown in Fig. 1, with the extent of the two
182 strips displayed. The ArcticDEM for all samples in this paper refers to this mosaiced dataset.
183 Land use and land cover (LULC) for Helsinki was acquired from the CORINE Urban Atlas
184 2012 database (<https://land.copernicus.eu/local/urban-atlas/urban-atlas-2012>). This LULC
185 features 22 land cover types in Helsinki. In this paper, features were merged to four categories:
186 urban, forest, open land, and water. Details of this reclassification of the LULC data can be
187 found in Supplement Table S1.



188

189 **Figure 1.** Locations of the three studied samples (S1, S2 and S3) within the city of Helsinki are shown at a).
190 Elevation values of the ArcticDEM at S1, S2 (overlain with transects crossing), and at S3 are shown in b), c), d)
191 respectively. Locations of coastal areas, lakes and rivers are also labelled. The ArcticDEM strip data is acquired
192 from the Polar Geospatial Center at <https://data.pgc.umn.edu/elev/dem/setsm/ArcticDEM/mosaic/v3.0/2m/>. The
193 water body outlines were acquired from the Finnish Environment Institute at
194 https://www.syke.fi/enUS/Open_information/Spatial_datasets/Downloadable_spatial_dataset.

195 3 Methods

196 3.1 Morphological filters

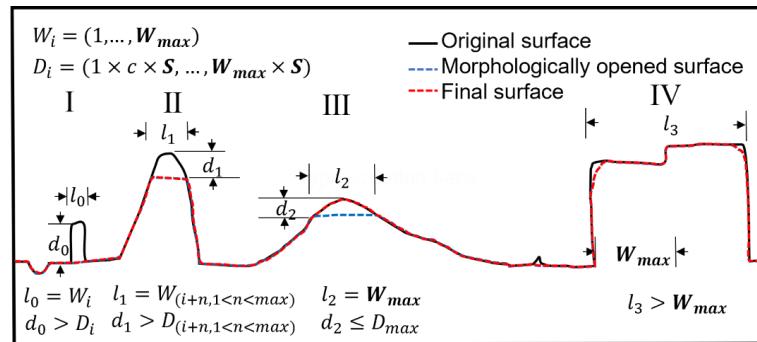
197 The generation of bare-earth ArcticDEM (our version of ArcticDEM with artefacts
198 removed) was conducted by employing two different morphological filters: PMF and SMRF
199 separately. They are considered because of their reported effectiveness in filtering LIDAR
200 point clouds, simple conceptualized parameters, and the fact that they are open access.

201 The PMF was designed to remove non-ground measurements (buildings, vegetation,
202 vehicles) from airborne LIDAR data (Zhang et al., 2003). It consists of an object detection and
203 an interpolation process which employs non-object pixel elevations to generate the values of
204 the object pixels. The PMF provides an advance on the morphological filter algorithm (Kilian



205 et al., 1996) by enabling a gradually increasing window width to detect non-ground objects
206 regardless of their size. In addition, an elevation difference threshold based on elevation
207 variations of the terrain, buildings, and trees was introduced to preserve the terrain. The
208 maximum window size and elevation variation threshold parameters control the filtering
209 process (more details can be found at Zhang et al., 2003).

210 More recently, a SMRF was proposed by Pingel et al (2013), also with the aim of
211 removing non-ground measurements from airborne LIDAR data. While the SMRF follows a
212 similar two-step process to the PMF, the approaches taken to detect objects and interpolate
213 elevation values of objects are different. SMRF adopts a linearly increasing window (as
214 opposed to the exponential increase of PMF) and simple slope thresholding, along with a novel
215 image inpainting technique. Like the PMF, the maximum window size (W_{max}) and slope
216 threshold (S) (equivalent to the elevation variation threshold of PMF) parameters control the
217 performance of the filter (Fig. 2). The core of the filter is the object detection where
218 morphological opening is applied to the original surface based on the current window size (W_i)
219 increasing from one pixel, by one pixel, to the maximum window size (in distance units, meters
220 in this research). For each window size within the range, the difference between the original
221 surface ($W_i=1$) or the surface from the last step ($W_i>1$) and the morphologically opened surface
222 is calculated and this difference (for example, d_0 , d_1 , d_2 in Figure 2) is compared with the
223 current difference threshold (D_i) (defined as the slope threshold S multiplied by the current
224 window size W_i) to determine whether the object flag of the pixel should be accepted or
225 rejected. When the difference is smaller than the current difference threshold (D_i), the object
226 flag of these pixels is rejected (Fig.2 III) and the elevated areas are retained. Otherwise, pixels
227 are flagged as objects and then interpolated (Fig.2 I, II). When the maximum window size is
228 smaller than the patch size of the elevated areas (for example, l_3), the morphological opening
229 will be unsuccessful, and elevations in that patch area remain almost identical to the original
230 elevation (Fig.2 IV).



231

232 **Figure 2.** Illustration of the SMRF filtering process in a simplified urban environment with artefacts (I, IV) and
 233 hills (II, III). The symbols are W: window size, D: difference threshold, C: cell size (C equals 2 m in this case),
 234 S: slope threshold, l: patch size of the elevated areas.

235 3.2 Optimal filter selection and error evaluation of the ArcticDEM-SMRF realizations

236 At Sample S1 and S2, combinations of a range of window size (i.e., maximum window
 237 size) and slope threshold parameters were tested for both the PMF and SMRF filters (Table 1).
 238 The optimal filter was identified as the resultant DEMs with the smallest error (Root Mean
 239 Square Error, i.e., RMSE) filtered using PMF and SMRF respectively (details are presented in
 240 Sect. 4.1). Then, the best performing filter (SMRF) was applied to Sample S3 with a range of
 241 window size and slope threshold parameters (Table 1), which generated a total of 234 filtered
 242 ArcticDEM realizations, hereafter called ArcticDEM-SMRF. Using the LIDAR DTM as the
 243 reference, the RMSE and Mean error of the ArcticDEM-SMRF realizations as well as the
 244 reduction of RMSE over the original ArcticDEM-SMRF was calculated at pixel level (2 m)
 245 (Eq. (1)-(3) and Text S1 in the Supplement). Due to other possible error sources, like shadow
 246 effects in the photogrammetry DEM, the calculations excluded values outside the 2.5th and
 247 97.5th percentile as outliers. The ArcticDEM-SMRF with the lowest RMSE for all land areas
 248 among the realizations is termed the optimal ArcticDEM-SMRF. The three error metrics of the
 249 ArcticDEM-SMRF realizations were analyzed against the window size and the slope threshold
 250 parameter to examine the effectiveness of the SMRF filter at removing artefacts. As the
 251 artefacts of S3 are a mixture of buildings and vegetation, the filter effectiveness to these
 252 parameters was analyzed separately for all land areas, only urban areas, and only forest areas.

253

254

255



256

Table 1. Key parameter settings of the morphological filters tested in the three samples.

Filter	Sample	Key Parameters			
		Window size (m)		Slope threshold	
		range	interval	range	interval
PMF	S1	10-66	4	0.1-0.3	0.2
	S2	10-66	4	0.1-0.3	-
SMRF	S1	10-50	2	0.01-0.1	0.005
	S2	10-50	2	0.01-0.1	0.005
	S3	10-180	10	0.03-0.15	0.01

257 * The unit of the slope threshold values shown here is radian for PMF, percent for SMRF.

258

3.3 Flood inundation evaluation of the ArcticDEM-SMRF realizations

259

For the 192 km² area covered by Sample 3 simple pluvial models were built at 10 m spatial resolution instead of the original 2 m of the ArcticDEM due to computational cost considerations. These models use DEM inputs from the LIDAR DTM, the original ArcticDEM, and the ArcticDEM-SMRF realizations which were filtered with various parameter combinations of the SMRF filter, respectively. The LIDAR DTM simulation was used as the benchmark. For this computation the hydrodynamic model LISFLOOD-FP was used (Bates et al., 2010). The model solves the local inertial form of the shallow water equations in two dimensions across the model domain. For pluvial flood modelling, the model takes the terrain elevation and rainfall data as inputs, and uses a raster-on-grid approach to calculate the velocity, water depth, and inundation (Bates et al., 2021). The input DEMs were aggregated to 10 m by averaging before being used in the flood simulation. For the ArcticDEM and ArcticDEM-SMRF models, elevation values in coastal areas (covered by water) were replaced with the LIDAR DTM values. This was done to remove the impact of the DEM error in non-land areas on the simulation. Rainfall data were acquired from the Climate Guide of Finland at <https://www.klimatguiden.fi/articles/database-of-design-storms-in-finland>. It provides the database of design storms with the real momentary variations in intensity for locations across Finland. This database was generated based on radar measurements and derivations. An extreme rainfall with a duration of 3 h and a return period of 500 years was used in the simulation. This was selected to minimize the simulation time while ensuring that the difference between the simulations was distinguishable. Under this duration and return period conditions, the precipitation data at the nearest station (60.04°N, 102.54°E) to the city of Helsinki was used. The precipitation is 102.54 mm in total with peak intensity at 182.4 mm/h.

280



281 The simulation results were compared to the LIDAR DTM benchmark in terms of the
282 simulated flood extent using the Critical Success Index (CSI) score, the Hit Rate, and the False
283 Alarm Ratio (FAR) defined by Eq. (1) - (3) (Wing at al., 2017), and the water depth errors
284 using the RMSE and the Mean error, Eq. (4) and (5). A wet cell is defined as one with simulated
285 water depth exceeding 0.1 m in this paper. As is typical in often the case in pluvial simulations,
286 small isolated wet areas (where the number of connected wet cells was less than 15) were
287 excluded from both the benchmark model (LIDAR) and the evaluation target models
288 (ArcticDEM and ArcticDEM-SMRF) before calculating the metrics. First, all five metrics
289 using the set of ArcticDEM-SMRF DEMs derived using different filter parameters were
290 compared with the flooding performance of the original ArcticDEM. Then, the relationship
291 between the five flooding metrics and the RMSE and Mean error of the DEM of the
292 ArcticDEM-SMRF realizations (aggregated at 10 m) was depicted for all land areas, urban and
293 forest areas individually. Furthermore, the flooding performance simulated by the optimal
294 ArcticDEM-SMRF was evaluated spatially.

295
$$CSI = \frac{A}{A+B+C} \quad (1)$$

296
$$Hit\ Rate = 100\% \times \frac{A}{A+C} \quad (2)$$

297
$$FAR = 100\% \times \frac{B}{A+B} \quad (3)$$

298
$$RMSE_{water\ depth} = \sqrt{\frac{\sum_{i=1}^{i=n} (WD_{i,C,DEM} - WD_{i,C,LIDAR})^2}{n}} \quad (4)$$

299
$$Mean\ error_{water\ depth} = \frac{\sum_{i=1}^{i=n} (WD_{i,C,DEM} - WD_{i,C,LIDAR})}{n} \quad (5)$$

300 *A is the number of pixels which are wet in both the DEM and the LIDAR simulation, i.e., where the two models
301 agree; B is the number of pixels which are wet in the DEM simulation but not the LIDAR simulation, i.e.,
302 overestimation; C is the number of pixels which are wet in the LIDAR simulation but not the DEM simulation,
303 i.e., underestimation.

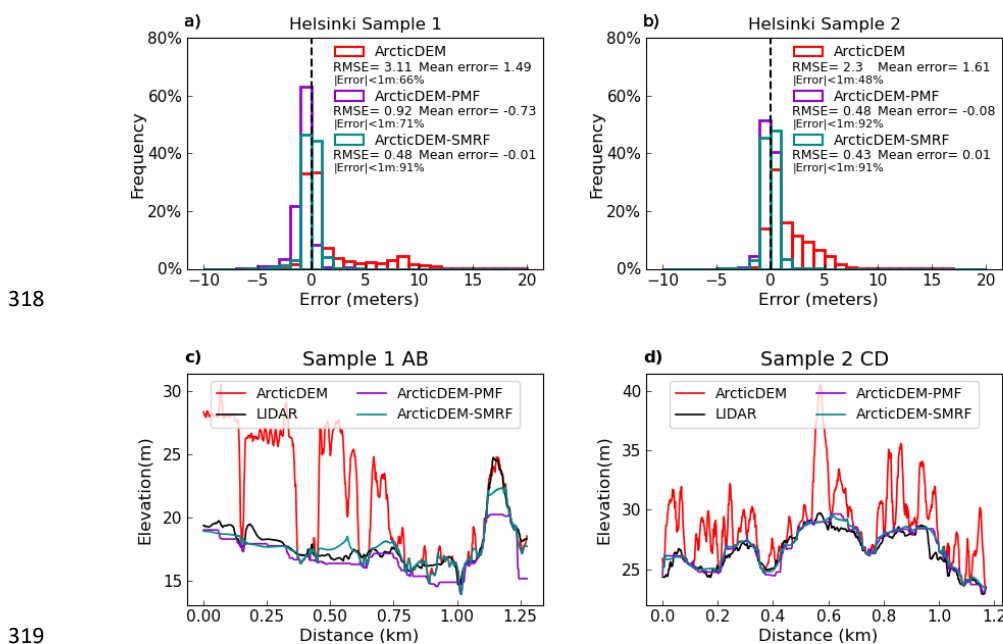
304 * $WD_{i,DEM}$ is the water depth at pixel i simulated using the DEM (ArcticDEM-SMRFs or the original ArcticDEM
305 depending on the calculation target), and n is the number of the wet cells (wet in either the LIDAR or the DEM
306 simulation) within category C. Category C is defined by the land use and land cover, and they can be all land
307 areas, urban, forest. For example, the water depth RMSE of ArcticDEM-SMRF in urban areas are calculated based
308 on the ArcticDEM-SMRF pixels within urban areas.



309 **4 Results**

310 4.1 Optimal filter selection

311 The effect of using the PMF and SMRF filters to remove artefacts from the ArcticDEM
312 in the two building-dominated samples S1 and S2 is evaluated by plotting the error distribution
313 and transect profiles. The filtered ArcticDEM with the smallest RMSE using each filter's
314 optimum parameters is shown in Fig. 3. The optimal PMF parameters for S1 and S2 are window
315 size = 42 m, 30 m, slope threshold = 0.3 (radian) for both, and the optimal SMRF parameters
316 for S1 and S2 are window size = 32 m, 14 m, slope threshold = 0.08, 0.05 (%), respectively.
317 The calculation of error figures was conducted at 2 m pixel scale.



318
319
320 **Figure 3.** Error histograms of ArcticDEM, ArcticDEM with PMF applied (ArcticDEM-PMF) and ArcticDEM
321 with SMRF applied (ArcticDEM-SMRF) for sample S1, a) and S2, b). Profile of ArcticDEM, ArcticDEM-PMF,
322 ArcticDEM-SMRF, and LIDAR DTM for transects through S1, c) and S2, d). The location of transects is shown
323 in Fig. 1b and c.

324 The error histograms show that both PMF and SMRF can effectively remove much of
325 the bias caused by artefacts in ArcticDEM, with the resulting RMSE falling below 1 m in all
326 cases. The count of pixels with error <1 m increased to 91% in both samples. The SMRF filter
327 achieved a lower RMSE (0.48 m and 0.43 m for S1 and S2, respectively) compared to PMF



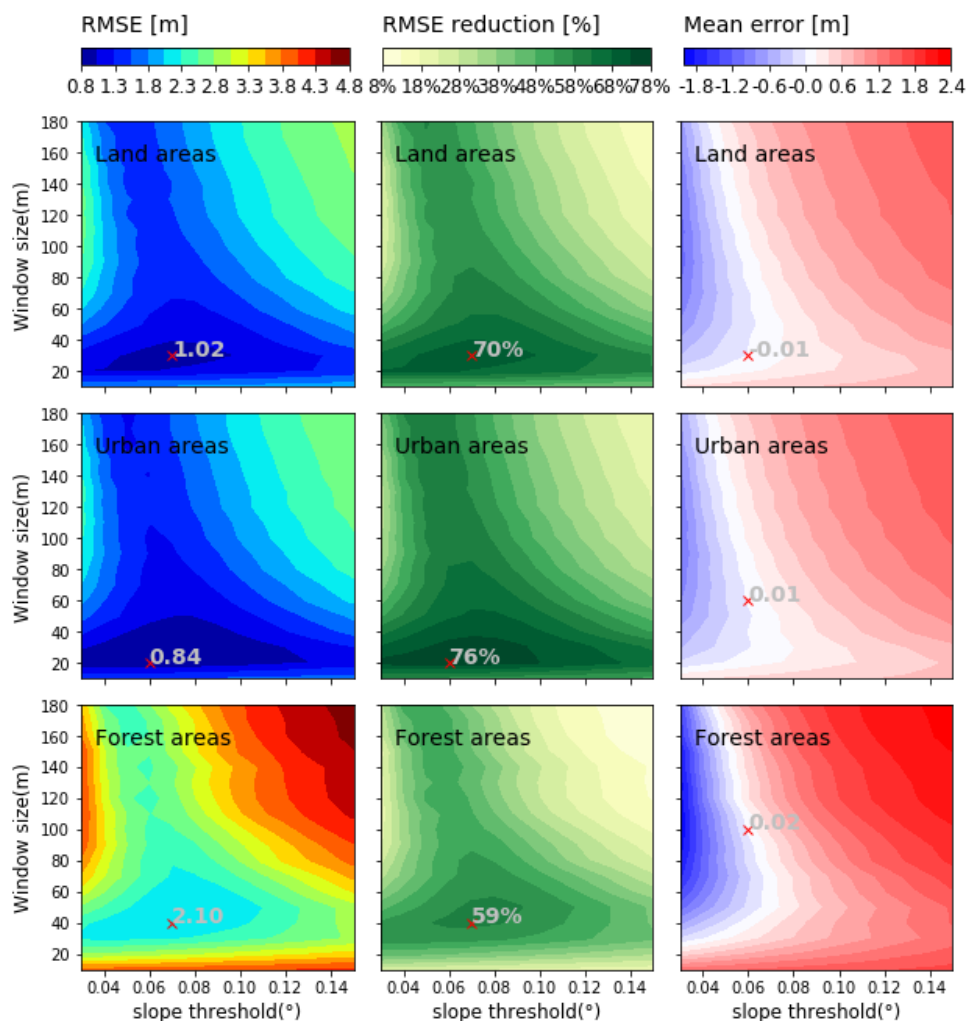
328 (0.92 m and 0.48 m) (Fig. 3a and b). The Mean error of the filtered DEMs for S1 and S2 also
329 evidences that SMRF has an advantage over PMF.

330 The DEM profile through S2 shows that SMRF and PMF work similarly well, while
331 the profile through S1 shows that SMRF can preserve more terrain details than PMF in
332 moderate hillslope areas (Fig. 3c, e.g., distance 0.75-1.0 km). However, both filters incorrectly
333 identified the steepest areas of S1 as artefacts, especially PMF (Fig. 3c distance 1.0-1.25 km).
334 Considering both the histogram and profile results, SMRF was selected as the optimal filter to
335 remove the artefacts from ArcticDEM for this site.

336 The sensitivity of the slope threshold and the window size parameter to the error metrics
337 for ArcticDEM-SMRF at sample S1 and S2 can be found in the Supplement Figure S1 and
338 Text S2.

339 4.2 Bare-earth DEM generation and its error evaluation

340 In order to understand the effectiveness of the SMRF in a more complex urban
341 environment the error metrics RMSE, RMSE reduction percentage and Mean error of the
342 ArcticDEM-SMRF realizations were computed for the larger sample S3. These metrics were
343 analyzed against the window size and slope threshold parameter of the SMRF filter to evaluate
344 the sensitivity of ArcticDEM-SMRF error to changes in these values. As the surface artefact
345 bias in S3 is mainly caused by buildings and forests, the analysis was conducted for all land
346 areas as well as for urban areas and forest areas separately (Fig. 4).



347

348 **Figure 4.** Surface plots of the slope threshold and the window size parameters of the SMRF filter against the
 349 RMSE, the RMSE reduction percentage and Mean error of the filtered DEM-ArcticDEM-SMRF for sample S3.

350 The location of the smallest values of the RMSE, the greatest values of the RMSE reduction and the smallest
 351 absolute values of the Mean error are marked as red crosses, with the values displayed. Parameter details can be
 352 found in Table 1.

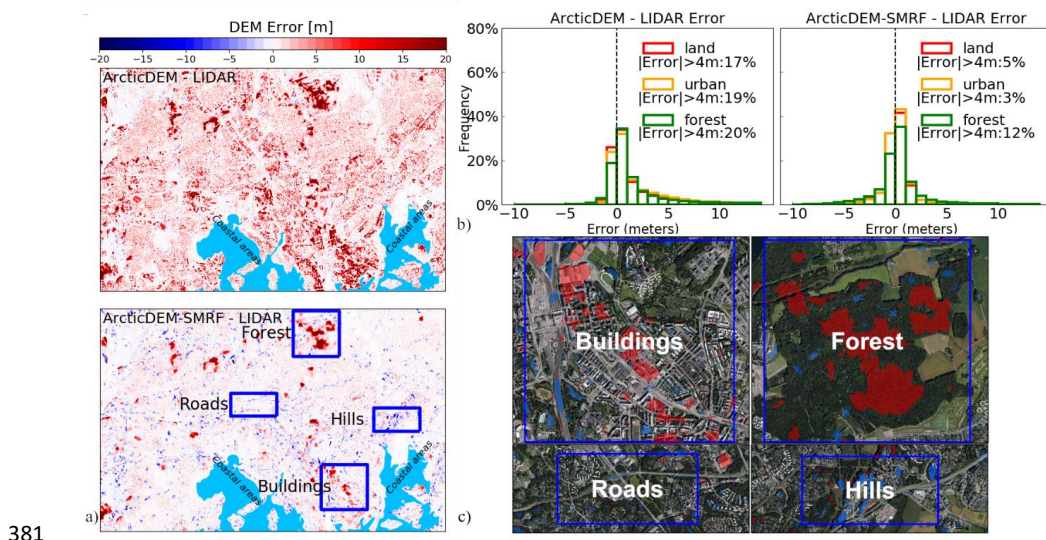
353 For area S3, the smallest RMSE of the ArcticDEM-SMRF realization is 1.02 m (i.e.,
 354 the optimal ArcticDEM-SMRF) within all land areas, 0.84 m in urban areas and 2.1 m in forest
 355 areas. These values represent 70%, 76% and 59% reductions of the ArcticDEM error
 356 respectively. The greatest reduction was achieved with a slope threshold of 0.07 combined with
 357 a window size of 30 m for all land areas or 40 m for forest areas, and a slope threshold of 0.06



358 with a window size of 20 m for urban areas. Although the RMSE of the optimal ArcticDEM-
359 SMRF is greater than that computed for samples S1 and S2 (Fig. 3a, b), the magnitude of the
360 error reduction indicates that the SMRF is still very effective at removing surface artefacts from
361 ArcticDEM for this larger sample. More than 40% of the 234 parameter combinations can
362 reduce the RMSE by greater than a half. Thus, the SMRF filter is considered as a robust filter
363 given that the tested parameters range are set generally broad.

364 This robustness also means that different combinations of window size and slope
365 threshold can achieve similar resultant RMSE (for example, for urban areas window size = 20
366 m with slope threshold between 0.03 and 0.12, or window size = 40 m with slope threshold
367 between 0.05 and 0.1). For sample S3, the most effective window size ranges from 20 m to 30
368 m for all land areas, from 20 m to 40 m for urban areas, and from 30 m to 60 m for forest areas
369 with slope threshold between 0.04-0.1. From the parameter selection perspective within the
370 effective range, a smaller window size is more robust and is therefore preferred because the
371 choice of the corresponding slope threshold is broader compared with a larger window size.
372 When the window size is smaller than 20 m, the error of the filtered DEM becomes almost
373 independent from the slope threshold parameter choice. With some parameter combinations
374 the SMRF becomes less effective at removing artefacts or introduces negative errors, which is
375 a combination of large slope threshold (> 0.1) and large window size (> 60 m) or when the
376 slope threshold is smaller than 0.04 with window size larger than 20 m. Additionally, when the
377 window size parameter is above 60 m, the Mean error of the filtered DEM becomes more
378 sensitive to the slope threshold, especially with slope threshold smaller than 0.06.

379 The error distribution of the optimal ArcticDEM-SMRF was also analyzed spatially
380 and statistically (Fig. 5).



381

382 **Figure 5.** a) Difference maps between the original ArcticDEM, the optimal ArcticDEM-SMRF (with slope
383 threshold = 0.07, window size = 30 m as the SMRF parameters) and the LIDAR DTM at 2 m. b) The error
384 histograms of the original ArcticDEM, the optimal ArcticDEM-SMRF, where the calculation was conducted at
385 2 m pixel level. In the bottom map of a), example locations of four features that relate to the residual errors of
386 the ArcticDEM-SMRF are labelled. The aerial image of these locations is shown in c) where areas with errors
387 exceeding 4 m were marked (> +4 m as red polygons and < -4 m as blue polygons, in 50% transparency). The
388 aerial image is orthophotograph of Helsinki with a horizontal resolution at 8 cm, acquired during growing
389 season of 2017, which was accessed from Helsinki Region Infoshare at
390 https://hri.fi/data/en_GB/dataset/helsingin-ortoilmakuva.

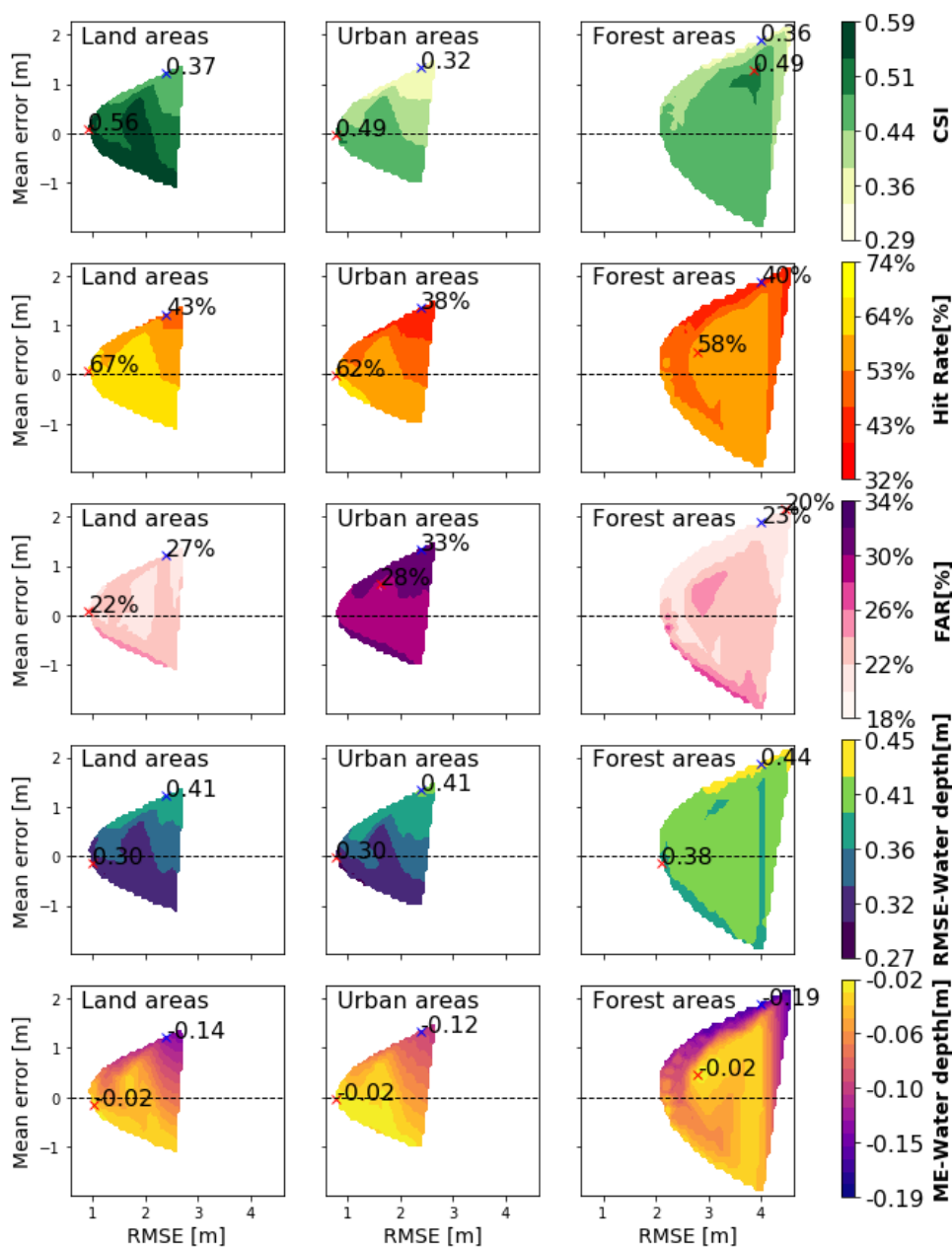
391 The error maps before and after applying the filter show that the SMRF method largely
392 reduces the errors in ArcticDEM, especially in urban areas (Fig. 5a, b). Although some residual
393 errors (> 4 m) are present in the optimal ArcticDEM-SMRF, they comprise a very small
394 percentage (~5%) of the whole area (Fig. 5b). Errors in dense forest areas and for closely spaced
395 buildings with large floor areas typically present as the largest positive residual errors as shown
396 in Fig. 5c. Large negative errors occur in hillslope areas (usually slope >10°) and in some areas
397 where above-ground traffic links such as junctions, viaducts, or overpasses are present (Fig.
398 5c).

399 4.3 Flood inundation evaluation of the ArcticDEM-SMRF realizations

400 The flooding evaluation metrics simulated using the original ArcticDEM and the
401 ArcticDEM-SMRF realizations for all the 234 parameter combinations are plotted against the



402 DEM error metrics (RMSE, Mean error calculated at 10 m) for each DEM realization in Fig.
 403 6. This analysis was conducted for all land areas, urban and forest areas separately.



404

405 **Figure 6.** Surface plot of the CSI score, Hit Rate, FAR, the water depth RMSE and Mean error (ME) simulated
 406 using the ArcticDEM-SMRF realizations (ArcticDEM filtered using the 234 SMRF parameter combinations) at
 407 sample S3 plotted against the RMSE and the Mean error of each realization member. The location of the highest



408 CSI and Hit Rate, the smallest FAR, RMSE and the smallest absolute value of mean water depth error are
409 marked as red crosses, with the values displayed. In addition, the RMSE, Mean error of the original ArcticDEM
410 are located and marked as blue crosses in each panel with the five metrics value of the original ArcticDEM
411 simulation displayed.

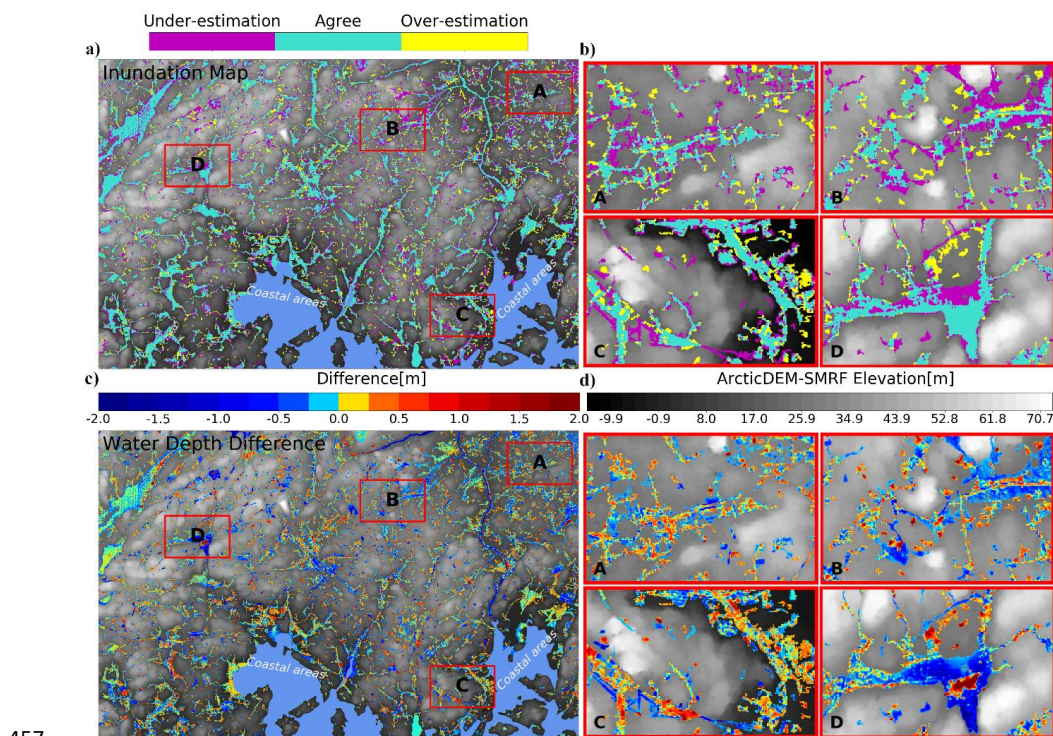
412 As a result of the reduced RMSE and Mean error the flooding performance of
413 ArcticDEM-SMRF improved for almost all the parameter combinations. For the whole S3 area,
414 the CSI score increased by 0.19, achieving a maximum value of 0.56 against the benchmark
415 LIDAR simulation. CSI increased by 0.17 in urban areas (to 0.49), and by a slightly smaller
416 amount of 0.13 in forest areas (to 0.49). It should be noted that although residual errors of
417 ArcticDEM-SMRF in urban areas are not as large as in other areas, the flooding extent
418 prediction skill doesn't exceed a CSI of 0.5. This is likely because the flooding extent for a
419 pluvial simulation becomes very sensitive to the small-scale errors of the DEM in flat areas
420 where water depths are typically extremely shallow. In this sense, simulation of pluvial
421 flooding is a rigorous test of DEM quality and the results achieved here using ArcticDEM-
422 SMRF should be interpreted with this in mind. It is also important to remember that the LIDAR
423 data, whilst good, is not truth, and has a reported vertical error of 0.3 m. LIDAR noise and
424 systematic error also contribute to some of the difference between the flooding performance of
425 models using the LIDAR and ArcticDEM-SMRF data. Simulations of fluvial flooding, where
426 depths are typically greater, would likely score higher on the spatial extent performance
427 metrics. The Hit Rate was improved by an even larger amount: 24, 24 and 18 percentage points
428 in all land areas, urban areas, and forest areas, respectively. The FAR was reduced by 5
429 percentage points in all land and urban areas, 3 percentage points in forest areas. The greater
430 improvement in urban areas provides evidence that the filter is especially effective at improving
431 the flood simulation in urban areas, considering that flooding in urban areas is usually more
432 fragmented and thus is more difficult to predict than in forest areas. With the ArcticDEM-
433 SMRF, the simulated water depth error (RMSE) was reduced by up to 0.11 m for all land areas
434 and urban areas compared to the original ArcticDEM, and this reduction was slightly smaller
435 (0.06 m) in forest areas. Although the water depth is still underestimated, the ArcticDEM-
436 SMRF simulation reduced the average error by 0.12 - 0.17 m compared to that of the original
437 ArcticDEM. Unlike the flooding extent performance comparison between urban and forest
438 areas, the water depth error in urban areas is always smaller than in forest areas in both the
439 simulation with the original ArcticDEM and the ArcticDEM-SMRF realizations. This is a
440 result of the smaller DEM error in urban areas. Thus, it can be inferred that the water depth



441 error is more sensitively impacted by the error of the DEM than the flood extent, at least in the
442 case of these pluvial flooding simulations.

443 Unsurprisingly, the ArcticDEM-SMRF with the smallest vertical elevation error
444 achieved the best flooding performance for all land areas. However, there are two other cases
445 where equally good flooding performance can be simulated using ArcticDEM-SMRF with
446 larger error. The first case occurs when the DEM is over-corrected by the filter, i.e., where
447 negative errors are present in the filtered DEM. In this case, some steep areas are identified as
448 objects and are flattened incorrectly. As these are not prone to be flooded, the flooding
449 performance is barely impacted. The second case occurs when the DEM preserves the most
450 terrain details, shown at the spike areas in Fig. 6 (ArcticDEM-SMRF mean error of >-0.5 m
451 and CSI between 0.54 and 0.59 for land areas). This implies that for flood simulation the
452 filtering strategy can perform equally well by aiming to achieve the lowest DEM error, or by
453 removing the artefacts as much as possible (over-filtering), or by preserving the terrain details
454 as much as possible (filtering with a small window size of 10 m in this case study).

455 The spatial distribution of the flooding extent and water depth error simulated using the
456 optimal ArcticDEM-SMRF is shown in Fig. 7.





458 **Figure 7.** Inundation extent simulated using the optimal ArcticDEM-SMRF parameters (slope threshold = 0.07,
459 window size = 30 m) at 10 m, where inundation areas that agree with, overpredict and underpredict the extent of
460 the LIDAR DTM 10 m simulation are shown at a). The water depth difference between the ArcticDEM-SMRF
461 and LIDAR DTM simulations for all wet cells is shown at c). Areas with significant disagreement are marked
462 by rectangles denoted A, B, C, D with the zoomed in maps displayed at b) and d). The land cover of A and C is
463 building-dominated, and forest-dominated at B and D.

464 For a 10 m spatial resolution simulation, ArcticDEM-SMRF can capture the major
465 flooded areas correctly with underestimation mainly around the edge of the agreed wet cells
466 and with overestimation presenting as scattered, small patches. Total underestimated area was
467 about 1.8 times greater than that of overestimated areas. Underestimation disproportionately
468 occurred along traffic links and along the edge of streams, in lake areas as well as in some of
469 the forest areas with significant residual errors (Fig. 7a).

470 Unlike the general underestimation for the domain as a whole, both underestimation
471 and overestimation were present in urban areas and the number of pixels that are under- and
472 over-estimated is similar. These errors appear as disconnected patches with smaller size and
473 their spatial distribution is more even compared to errors in forest areas (Fig. 7b-A, C in
474 contrast to Fig. 7b-B, D).

475 The greatest water depth error is present in forest areas (Fig. 7d-B, D) where the
476 ArcticDEM-SMRF simulation either fails to inundate these areas (underestimation) or
477 generates much shallower water depths compared to that simulated using the LIDAR DTM. In
478 urban areas, the water depth error simulated using the ArcticDEM-SMRF is relatively small,
479 varying between -0.5 m and 0.5 m (Fig. 7d-A, C).

480 5 Discussion

481 5.1 The selection ArcticDEM strips

482 The error of different ArcticDEM strips covering the same areas could vary
483 significantly. In this study site, we found that the main difference in error occurs in forest areas.
484 Within a selected 11 km² forest area the error of the strip acquired on the 16th of February 2015
485 is 12.2 m, while within the same area that of the strip acquired on the 14th of March 2013 was
486 much smaller (6.66 m). From air photos, no noticeable forest coverage change was found
487 within the selected areas between the acquisition years of the two strips. Therefore, the
488 difference between strips could be caused by the leaf-on/off differences or the snow situation.
489 In this case, since both acquisition dates are during leaf-off season it is likely a result of



490 differences in snow cover. Even for the building dominated samples, the error at S1 and S2 of
491 the former strip (acquired on the 16th of February 2015) is 0.31 m, and 0.88 m larger than the
492 latter strip. Thus, we suggest that for general bare-earth generation from ArcticDEM, different
493 strips should consider the forest characteristics (evergreen or deciduous) and the weather
494 conditions (snow free or not) on the data acquisition date in overlapping areas. Strip data in
495 leaf-off and snow-free conditions will represent more of the ground elevation compared to data
496 collected in leaf-on or snow-covered conditions. Also, snow-free condition avoids the feature
497 matching difficulty between stereo images in the DEM generation process, which happens
498 often because the presence of snow results in low-contrast and repetitive image textures (Noh
499 and Howat, 2015). The snow condition on the strip data acquisition date can be checked using
500 the daily MODIS snow index product (Hall et al., 2016).

501 5.2 SMRF filter parameters

502 A direct application of the SMRF filter proved to be effective at removing most of the
503 surface artefacts at this study site, especially for buildings. It means that this LIDAR processing
504 tool can be employed without modification in generating a bare-earth ArcticDEM in urban
505 areas with buildings spacing at medium density like Helsinki (0.22 floor area ratio on average
506 within a 250 m grid cell, https://hri.fi/data/en_GB/dataset/rakennustietoruudukko). The SMRF
507 is generally robust to its window size and slope threshold parameter choices with respect to the
508 error reduction of the filtered ArcticDEM and the reduction could be optimized by narrowing
509 the parameters to certain values. Although by the algorithm definition, the parameters should
510 be set as the largest patch size and the greatest terrain variation, this research shows that in a
511 large domain application the window size and the slope threshold parameter range should be
512 gauged around the median value of the artefacts patch sizes and of the terrain variation values.
513 At this study site, the range of the window size is 20 - 40 m and a range of 0.04 - 0.1 for the
514 slope threshold performed best, with optimal values located at the median point of the
515 distribution. Within the reasonable range, a smaller window size proved to be more robust in
516 that it will be less sensitive to the choice of the slope threshold.

517 When benchmarking to a LIDAR DTM simulation, similarly good flood simulation
518 performance for the filtered DEMs is found to be achieved by the ArcticDEM-SMRF with
519 smallest error, or negatively biased ArcticDEM-SMRF or positively biased ArcticDEM-SMRF
520 preserving the most terrain details. Applying the SMRF filter is a trade-off between the removal
521 of artefact errors and the loss of terrain detail. When the SMRF is applied with a small window



522 size (such as 10 m), most of the terrain details can be maintained in the ArcticDEM-SMRF
523 while the residual error of the DEM can be large as a result of the residual artefacts with large
524 patch sizes. Since these preserved terrain details might be important in the inundation
525 simulation, the flood performance could be better in some places than when more of the
526 residual errors are removed at the cost of losing these details. Whilst the SMRF filter tends to
527 produce negative errors on hillslopes, these areas are not flooding-prone so the flooding
528 inundation is not significantly affected. The error sensitivity of the ArcticDEM-SMRF
529 realizations to the SMRF parameters at different slope areas is included in the Supplement as
530 Figure S2 and Text S3. Despite the above points, the filter parameters of the two latter cases
531 are not easy to gauge and likely to varying from location to location, thus using the median
532 values of the artefacts size and terrain variation is suggested.

533 5.3 Limitations

534 Although the SMRF filter successfully removed most of the ArcticDEM errors caused
535 by artefacts, there is a small percentage of artefact errors (~5%) that remains in dense built-up
536 areas and in large vegetation patches. Pixels in these areas are not entirely flagged as objects
537 with a window size of 30 m and some pixels are instead wrongly designated as ‘ground’ values
538 in the interpolation. Even though with an enlarged window size the remaining artefact errors
539 could be removed by the SMRF, the interpolation over large patch areas would potentially be
540 unsuccessful due to a lack of ground elevations within these zones. Additional data or a tailored
541 approach is required to achieve the desired result in areas with large patch sizes. For building
542 artefacts, the OpenStreetMap building footprint data could be helpful to predefine the areas of
543 objects. The ICESAT2 terrain elevation might be useful to provide additional ground elevations
544 in forest areas with large patch sizes (Neuenschwander et al., 2020; Tian and Shan, 2021).

545 With this filter, artefacts with small size are usually identified before the window size
546 reaches the maximum and the subsequent interpolation is also more successful. This makes the
547 SMRF filter more effective at removing building artefacts than vegetation due to the general
548 smaller size of building patches. However, some desired features that present similar elevated
549 characters to building artefacts (such as traffic junctions or levees) might be removed by the
550 filter unfavorably, and negative errors are shown in these areas. It becomes very tricky to
551 preserve these feature heights by any automatic filtering approaches without the location
552 information of the features. With more sophisticated method, likely with some ancillary data,
553 this could be possible (Wing et al., 2019). For hilly areas, some of the natural terrain might be



554 identified as artefacts by the SMRF incorrectly and the subsequent interpolation can cause the
555 loss of terrain details. The error histograms and analysis of the ArcticDEM-SMRF generated
556 with different window size parameters at buildings and forest with large patch size, hillslope,
557 and roads examples can be found in Figure S3 and Text S4 in the Supplement. Thus, in terms
558 of the bare-earth DEM generation, the filter is likely to be less effective for areas with densely
559 packed artefacts or hilly areas.

560 For flood simulation the errors in ArcticDEM-SMRF along river channels and over
561 floodplains is particularly critical, and further DEM processing here could lead to additional
562 improvements. In the ArcticDEM-SMRF, the elevations of the river sections that run through
563 large patches of forest are positively biased because of the reduced effectiveness of the SMRF
564 filter in these areas. The water depth error along the river network is expected to be mitigated
565 once these blockages are removed, such as by using quantile regression techniques
566 (Schwanghart et al., 2017). Similarly, elevation values along the road network (acquired from
567 OpenStreetMap) were particularly interesting and extracted for further analysis. It was found
568 that the SMRF filter largely lowered the elevation of the road network where artefacts are
569 present. But the resulting DEM from SMRF is interpolated based on all neighbouring pixels
570 and not only along the road pixels on either side of the artefact removed. Thus, an unsmooth
571 distribution of the along-road elevation was generated, which is not ideal for flood simulation
572 and likely to be inaccurate. A linear interpolation along the central line of the road network
573 with a buffering around that could be used to reduce these errors in the future. It should be
574 noted that the buffering width of the central line of roads could be tricky to define when there
575 is not accurate road width data available.

576 Moreover, sinks can be present in ArcticDEM (areas with substantially lower elevation
577 than neighbouring pixels), possibly because of the shadow effect which is a common issue for
578 photogrammetry DEMs (Noh and Howat, 2015). These sinks should be identified and filled in
579 future work.

580 **6 Conclusions**

581 In this paper, we examine two morphological filters (PMF, SMRF) for removing
582 surface artefacts from the ArcticDEM strip data in a complex urban environment using the city
583 of Helsinki as a case study. We then assess the improvement in flood inundation simulation
584 provided by the filtered ArcticDEM relative to a LIDAR DTM benchmark in a pluvial flooding
585 scenario. To our knowledge, it is the first examination of the approach to generate bare-earth



586 ArcticDEM data specifically for flood applications. It was found that the SMRF performs better
587 at removing surface artefacts from ArcticDEM than the PMF filter, and it is robust to its
588 parameter setting. The optimal parameter combination is around the median value of the patch
589 size distribution of the artefacts and of the terrain variation, which resulted in an optimal
590 window size of 30 m and slope threshold of 0.07 in the city of Helsinki. With SMRF, the overall
591 error of the ArcticDEM can be reduced by up to 70% with the optimized parameters, achieving
592 a final RMSE of 1.02 m.

593 The flood inundation simulation performance of a standard two-dimensional
594 hydrodynamic model was considerably improved when using the filtered ArcticDEM in that
595 40% of the underestimated areas simulated by the ArcticDEM were eliminated. Although the
596 flooding extent performance simulated by the ArcticDEM-SMRF is still not a strong match to
597 the LIDAR DTM benchmark (CSI=0.56, although some of this difference will be caused by
598 errors in LIDAR itself), the pluvial flood simulation should be seen as a rigorous test as the
599 inundated areas usually vary within few pixels in urban areas and are easily impacted by small-
600 scale errors. The simulated water depth error of the optimal ArcticDEM-SMRF model is
601 comparable to the likely error of the LIDAR DTM simulation, as a result of ~0.1 m
602 improvement comparing to the original ArcticDEM.

603 The residual errors of the filtered ArcticDEM are mainly composed of: 1) positive
604 errors for artefacts with large patches sizes, which are not entirely removed by the filter; and
605 2) negative errors in hilly areas which are incorrectly identified as artefacts. Thus, when using
606 the SMRF filter in other study areas where the artefacts have a much higher density or artefacts
607 with a large patch size comprise a significant proportion of the study area, the effectiveness of
608 the SMRF filter could be less significant compared to the results of this study. Some
609 modification of the SMRF filter might be able to remove the densely distributed artefacts and
610 auxiliary data are likely to be needed to guarantee satisfying interpolation results. Applying the
611 SMRF filter to hilly areas is also likely to yield a less effective performance. From the
612 perspective of flood inundation simulation, the SMRF parameters should be configured
613 towards optimizing their range to generate the DEM with the lowest error.

614 This paper suggests that applying the SMRF without any algorithm modification is
615 effective to generate bare-earth DEMs from ArcticDEM and are likely to be applicable to other
616 high-resolution photogrammetry DEMs and other application areas. The generated bare-earth
617 DEM shows largely reduced error comparing to the original ArcticDEM and comparable
618 simulated water depth error to the LIDAR benchmark. Thus, it is a promising alternative to



619 LIDAR data for locations where such data are either not available or would not be cost efficient.
620 In the future, using ancillary data to address the residual errors of the filtered DEM should be
621 integrated to the bare-earth ArcticDEM generation process. To facilitate the use of bare-earth
622 ArcticDEM in flood simulation, the blockage of residual error within rivers and errors along
623 road network should be carefully treated.

624 **Data and code availability**

625 LIDAR data at 2 m was acquired from
626 <https://tiedostopalvelu.maanmittauslaitos.fi/tp/kartta?lang=en>. The error description of the
627 LIDAR data can be found at [https://www.maanmittauslaitos.fi/en/maps-and-spatial-](https://www.maanmittauslaitos.fi/en/maps-and-spatial-data/expert-users/product-descriptions/elevation-model-2-m)
628 [data/expert-users/product-descriptions/elevation-model-2-m](https://www.maanmittauslaitos.fi/en/maps-and-spatial-data/expert-users/product-descriptions/elevation-model-2-m). The quasigeoid heights was
629 downloaded from [https://www.maanmittauslaitos.fi/kartat-ja-paikkatieto/asiantuntevalle-](https://www.maanmittauslaitos.fi/kartat-ja-paikkatieto/asiantuntevalle-kayttajalle/koordinaattimuunnokset)
630 [kayttajalle/koordinaattimuunnokset](https://www.maanmittauslaitos.fi/kartat-ja-paikkatieto/asiantuntevalle-kayttajalle/koordinaattimuunnokset). The MODIS/Terra Snow Cover Daily L3 Global 500 m
631 SIN Grid, Version 6 data is available at <https://nsidc.org/data/MOD10A1/versions/6>. The
632 OpenStreetMap road network can be acquired at <https://overpass-turbo.eu/>. The building
633 density information of the city of Helsinki can be found at
634 https://hri.fi/data/en_GB/dataset/rakennustietoruudukko. The LISFLOOD-FP model is
635 available for non-commercial research purposes from
636 https://zenodo.org/record/4073011#_YeWAdP7P2UJ. The Bare-earth ArcticDEM can be
637 accessed at <https://doi.org/10.5523/bris.3c112q7u1x14a262m6z7hh0c4r>. The PMF algorithm
638 can be accessed at
639 <http://www.pylidar.org/en/latest/modules/pylidar/toolbox/grdfilters/pmf.html>, the SMRF
640 algorithm can be accessed at <https://github.com/thomaspingel/smrf-matlab>.

641 **Author contributions**

642 Yinxue Liu wrote the manuscript and carried out the data processing and analysis. Paul Bates
643 and Jeffery Neal provided comments on various drafts as well as advised on the analysis work.

644 **Competing interests**

645 The authors declare that there is no conflict of interest.

646 **Acknowledgements**

647 Yinxue Liu was supported by the China-Scholarship-Council (CSC) – University of Bristol
648 Joint PhD Scholarships Program. Paul Bates was supported by a Royal Society Wolfson
649 Research Merit award and UK Natural Environment Research Council grant NE/V017756/1.
650 Jeffrey Neal was supported by NE/S006079/1.

651 **References**

- 652 Archer, L., Neal, J. C., Bates, P. D., & House, J. I.: Comparing TanDEM - X data with frequently used DEMs for
653 flood inundation modeling, *Water Resour. Res.*, 54, 10-205, <https://doi.org/10.1029/2018WR023688>, 2018.
- 654 Bates, P. D., Horritt, M. S., & Fewtrell, T. J.: A simple inertial formulation of the shallow water equations for
655 efficient two-dimensional flood inundation modelling, *J. Hydrol.*, 387, 33-45,
656 <https://doi.org/10.1016/j.jhydrol.2010.03.027>, 2010.



- 657 Bates, P. D., Neal, J. C., Alsdorf, D., & Schumann, G. J. P.: Observing global surface water flood dynamics, in:
658 The Earth's Hydrological Cycle, Springer, 839-852, <https://doi.org/10.1007/s10712-013-9269-4>, 2013.
- 659 Bates, P. D., Quinn, N., Sampson, C., Smith, A., Wing, O., Sosa, J., ... & Krajewski, W. F.: Combined modeling
660 of US fluvial, pluvial, and coastal flood hazard under current and future climates, *Water Resour. Res.*, 57,
661 e2020WR028673, <https://doi.org/10.1029/2020WR028673>, 2021.
- 662 Ben-Haim, Z., Anisimov, V., Yonas, A., Gulshan, V., Shafi, Y., Hoyer, S., & Nevo, S.: Inundation modeling in
663 data scarce regions, arXiv [preprint], [arxiv:1910.05006](https://arxiv.org/abs/1910.05006), 2019.
- 664 Chen, Q., Gong, P., Baldocchi, D., & Xie, G.: Filtering airborne laser scanning data with morphological
665 methods, *Photogramm. Eng. Rem. S.*, 73, 175-185, <https://doi.org/10.14358/PERS.73.2.175>, 2007.
- 666 Chen, Z., Gao, B., & Devereux, B.: State-of-the-art: DTM generation using airborne LIDAR data, *Sensors*, 17,
667 150, <https://doi.org/10.3390/s17010150>, 2017.
- 668 Cui, Z., Zhang, K., Zhang, C., & Chen, S. C.: A cluster-based morphological filter for geospatial data analysis,
669 in: Proceedings of the 2nd ACM SIGSPATIAL International Workshop on Analytics for Big Geospatial Data, 1-
670 7, <https://doi.org/10.1145/2534921.2534922>, 2013.
- 671 DeWitt, J. D., Warner, T. A., Chirico, P. G., & Bergstresser, S. E.: Creating high-resolution bare-earth digital
672 elevation models (DEMs) from stereo imagery in an area of densely vegetated deciduous forest using
673 combinations of procedures designed for LIDAR point cloud filtering, *GISci. Remote Sens.*, 54, 552-572,
674 <https://doi.org/10.1080/15481603.2017.1295514>, 2017.
- 675 Faherty, D., Schumann, G. J. P., & Moller, D. K.: Bare Earth DEM Generation for Large Floodplains Using Image
676 Classification in High-Resolution Single-Pass InSAR. *Front. Earth Sci.*, 8, 27,
677 <https://doi.org/10.3389/feart.2020.00027>, 2020.
- 678 Garbrecht, J., & Martz, L. W.: Digital elevation model issues in water resources modeling. Hydrologic and
679 hydraulic modeling support with geographic information systems, 1-28. 2000, Available at
680 <https://proceedings.esri.com/library/userconf/proc99/proceed/papers/pap866/p866.htm>, last assess: 22 July, 2022.
- 681 Hall, D. K. and G. A. Riggs.: MODIS/Terra Snow Cover Daily L3 Global 500m SIN Grid, Version 6. Boulder,
682 Colorado USA, NASA National Snow and Ice Data Center Distributed Active Archive Center,
683 <https://doi.org/10.5067/MODIS/MOD10A1.006>, 2016.
- 684 Hawker, L., Bates, P., Neal, J., & Rougier, J.: Perspectives on digital elevation model (DEM) simulation for flood
685 modeling in the absence of a high-accuracy open access global DEM, *Front. Earth Sci.*, 6, 233,
686 <https://doi.org/10.3389/feart.2018.00233>, 2018.
- 687 Hawker, L., Uhe, P., Paulo, L., Sosa, J., Savage, J., Sampson, C., & Neal, J.: A 30m global map of elevation with
688 forests and buildings removed, *Environ. Res. Lett.*, 17, 024016, <https://doi.org/10.1088/1748-9326/ac4d4f>, 2022.
- 689 Hirano, A., Welch, R., & Lang, H.: Mapping from ASTER stereo image data: DEM validation and accuracy
690 assessment, *ISPRS J. Photogramm.*, 57, 356-370, [https://doi.org/10.1016/S0924-2716\(02\)00164-8](https://doi.org/10.1016/S0924-2716(02)00164-8), 2003.
- 691 Hu, F., Gao, X. M., Li, G. Y., & Li, M. DEM EXTRACTION FROM WORLDVIEW-3 STEREO-IMAGES AND
692 ACCURACY EVALUATION, *Int. Arch Photogramm.*, 41, <https://doi.org/10.5194/isprsarchives-XLI-B1-327-2016>, 2016.
- 693
- 694 Hui, Z., Hu, Y., Yevenyo, Y. Z., & Yu, X.: An improved morphological algorithm for filtering airborne LiDAR
695 point cloud based on multi-level kriging interpolation, *Remote Sens.*, 8, 35, <https://doi.org/10.3390/rs8010035>,
696 2016.
- 697 Jensen, J. L., & Mathews, A. J.: Assessment of image-based point cloud products to generate a bare earth surface
698 and estimate canopy heights in a woodland ecosystem, *Remote Sens.*, 8, 50, <https://doi.org/10.3390/rs8010050>,
699 2016.
- 700 Kulp, S. A., & Strauss, B. H.: CoastalDEM: A global coastal digital elevation model improved from SRTM using
701 a neural network, *Remote Sens. Environ.*, 206, 231-239, <https://doi.org/10.1016/j.rse.2017.12.026>, 2018.
- 702 Lakshmi, S. E., & Yarrakula, K.: Review and critical analysis on digital elevation models, *Geofizika*, 35, 129-
703 157, <https://doi.org/10.15233/gfz.2018.35.7>, 2018.
- 704 Liu, Y., Bates, P. D., Neal, J. C., & Yamazaki, D.: Bare - Earth DEM Generation in Urban Areas for Flood
705 Inundation Simulation Using Global Digital Elevation Models, *Water Resour. Res.*, 57, e2020WR028516,
706 <https://doi.org/10.1029/2020WR028516>, 2021.



- 707 Majasalmi, T., & Rautiainen, M.: Representation of tree cover in global land cover products: Finland as a case
708 study area, *Environ. Monit. Assess.*, 193, 1-19, <https://doi.org/10.1007/s10661-021-08898-2>, 2021.
- 709 Marconcini, M., Marmanis, D., Esch, T., & Felbier, A.: A novel method for building height estimation using
710 TanDEM-X data, in: 2014 IEEE Geoscience and Remote Sensing Symposium, 4804-4807, IEEE.
711 <https://doi.org/10.1109/IGARSS.2014.6947569>, 2014.
- 712 Mason, D. C., Horritt, M. S., Hunter, N. M., & Bates, P. D.: Use of fused airborne scanning laser altimetry and
713 digital map data for urban flood modelling, *Hydrol. Process.*, 21, 1436-1447, <https://doi.org/10.1002/hyp.6343>,
714 2007.
- 715 Meng, X., Wang, L., Silván-Cárdenas, J. L., & Currit, N.: A multi-directional ground filtering algorithm for
716 airborne LIDAR, *ISPRS J. Photogramm.*, 64, 117-124, <https://doi.org/10.1016/j.isprsjprs.2008.09.001>, 2009.
- 717 Moudrý, V., Lecours, V., Gdulová, K., Gábor, L., Moudrá, L., Kropáček, J., & Wild, J.: On the use of global
718 DEMs in ecological modelling and the accuracy of new bare-earth DEMs, *Ecol. Model.*, 383, 3-9,
719 <https://doi.org/10.1016/j.ecolmodel.2018.05.006>, 2018.
- 720 Neal, J. C., Bates, P. D., Fewtrell, T. J., Hunter, N. M., Wilson, M. D., & Horritt, M. S.: Distributed whole city
721 water level measurements from the Carlisle 2005 urban flood event and comparison with hydraulic model
722 simulations, *J. Hydrol.*, 368, 42-55, <https://doi.org/10.1016/j.jhydrol.2009.01.026>, 2009.
- 723 Neuenschwander, A., Guenther, E., White, J. C., Duncanson, L., & Montesano, P.: Validation of ICESat-2 terrain
724 and canopy heights in boreal forests, *Remote Sens. Environ.*, 251, 112110,
725 <https://doi.org/10.1016/j.rse.2020.112110>, 2020.
- 726 Noh, M. J., & Howat, I. M.: Automated stereo-photogrammetric DEM generation at high latitudes: Surface
727 Extraction with TIN-based Search-space Minimization (SETSM) validation and demonstration over glaciated
728 regions, *GISci. Remote Sens.*, 52, 198-217, <https://doi.org/10.1080/15481603.2015.1008621>, 2015.
- 729 O'Loughlin, F. E., Paiva, R. C., Durand, M., Alsdorf, D. E., & Bates, P. D.: A multi-sensor approach towards a
730 global vegetation corrected SRTM DEM product, *Remote Sens. Environ.*, 182, 49-59,
731 <https://doi.org/10.1016/j.rse.2016.04.018>, 2016.
- 732 Pingel, T. J., Clarke, K. C., & McBride, W. A.: An improved simple morphological filter for the terrain
733 classification of airborne LIDAR data, *ISPRS J. Photogramm.*, 77, 21-30,
734 <https://doi.org/10.1016/j.isprsjprs.2012.12.002>, 2013.
- 735 Porter, C., Morin, P., Howat, I., Noh, M. J., Bates, B., Peterman, K., ..., Bojesen, M., ArcticDEM, Harvard
736 Dataverse, V1, <https://doi.org/10.7910/DVN/OHHUKH>, 2018.
- 737 Rodriguez, E., Morris, C. S., & Belz, J. E.: A global assessment of the SRTM performance, *Photogramm. Eng.*
738 *Rem. S.*, 72, 249-260, <https://doi.org/10.14358/PERS.72.3.249>, 2006.
- 739 Rokhmana, C. A., & Sastra, A. R.: Filtering DSM extraction from Worldview-3 images to DTM using open source
740 software, in: IOP Conference Series: Earth and Environmental Science, 012054, <https://doi.org/10.1088/1755-1315/500/1/012054>, 2020.
- 742 Schubert, J. E., & Sanders, B. F.: Building treatments for urban flood inundation models and implications for
743 predictive skill and modeling efficiency, *Adv. Water Resour.*, 41, 49-64,
744 <https://doi.org/10.1016/j.advwatres.2012.02.012>, 2012.
- 745 Schumann, G. J., & Bates, P. D.: The need for a high-accuracy, open-access global DEM, *Front. Earth Sci.*, 6,
746 225, <https://doi.org/10.3389/feart.2018.00225>, 2018.
- 747 Schwanghart, W., & Scherler, D.: Bumps in river profiles: uncertainty assessment and smoothing using quantile
748 regression techniques, *Earth Surf. Dynam.*, 5, 821-839, <https://doi.org/10.5194/esurf-5-821-2017>, 2017.
- 749 Shean, D. E., Alexandrov, O., Moratto, Z. M., Smith, B. E., Joughin, I. R., Porter, C., & Morin, P.: An automated,
750 open-source pipeline for mass production of digital elevation models (DEMs) from very-high-resolution
751 commercial stereo satellite imagery, *ISPRS J. Photogramm.*, 116, 101-117,
752 <https://doi.org/10.1016/j.isprsjprs.2016.03.012>, 2016.
- 753 Sithole, G., & Vosselman, G.: Experimental comparison of filter algorithms for bare-Earth extraction from
754 airborne laser scanning point clouds, *ISPRS J. Photogramm.*, 59, 85-101,
755 <https://doi.org/10.1016/j.isprsjprs.2004.05.004>, 2004.
- 756 Tian, X., & Shan, J.: Comprehensive evaluation of the ICESat-2 ATL08 terrain product, *IEEE T. Geosci. Remote*,
757 59, 8195-8209, <https://doi.org/10.1109/TGRS.2021.3051086>, 2021.



- 758 Tan, Y., Wang, S., Xu, B., & Zhang, J.: An improved progressive morphological filter for UAV-based
759 photogrammetric point clouds in river bank monitoring, *ISPRS J. Photogramm.*, 146, 421-429,
760 <https://doi.org/10.1016/j.isprsjprs.2018.10.013>, 2018.
- 761 Trigg, M. A., Wilson, M. D., Bates, P. D., Horritt, M. S., Alsdorf, D. E., Forsberg, B. R., & Vega, M. C.: Amazon
762 flood wave hydraulics, *J. Hydrol.*, 374, 92-105, <https://doi.org/10.1016/j.jhydrol.2009.06.004>, 2009.
- 763 Wessel, B., Huber, M., Wohlfart, C., Marschalk, U., Kosmann, D., & Roth, A.: Accuracy assessment of the global
764 TanDEM-X Digital Elevation Model with GPS data, *ISPRS J. Photogramm.*, 139, 171-182,
765 <https://doi.org/10.1016/j.isprsjprs.2018.02.017>, 2018.
- 766 Wing, O. E., Bates, P. D., Neal, J. C., Sampson, C. C., Smith, A. M., Quinn, N., ... & Krajewski, W. F.: A new
767 automated method for improved flood defense representation in large-scale hydraulic models, *Water Res.*
768 *Res.*, 55, 11007-11034, <https://doi.org/10.1029/2019WR025957>, 2019.
- 769 Wing, O. E., Bates, P. D., Sampson, C. C., Smith, A. M., Johnson, K. A., & Erickson, T. A.: Validation of a 30
770 m resolution flood hazard model of the conterminous United States, *Water Resour. Res.*, 53, 7968-7986,
771 <https://doi.org/10.1002/2017WR020917>, 2017.
- 772 Yamazaki, D., Ikeshima, D., Tawatari, R., Yamaguchi, T., O'Loughlin, F., Neal, J. C., ... & Bates, P. D.: A high -
773 accuracy map of global terrain elevations, *Geophys. Res. Lett.*, 44, 5844-5853,
774 <https://doi.org/10.1002/2017GL072874>, 2017.
- 775 Yamazaki, D., Sato, T., Kanae, S., Hirabayashi, Y., & Bates, P. D.: Regional flood dynamics in a bifurcating mega
776 delta simulated in a global river model, *Geophys. Res. Lett.*, 41, 3127-3135,
777 <https://doi.org/10.1002/2014GL059744>, 2014.
- 778 Zaidi, S. M., Akbari, A., Gisen, J. I., Kazmi, J. H., Gul, A., & Phong, N. Z.: Utilization of Satellite-based Digital
779 Elevation Model (DEM) for Hydrologic Applications: A Review. *J. Geol. Soc. India*, 92, 329-336,
780 <https://doi.org/10.1007/s12594-018-1016-5>, 2018.
- 781 Zhang, K., Chen, S. C., Whitman, D., Shyu, M. L., Yan, J., & Zhang, C.: A progressive morphological filter for
782 removing nonground measurements from airborne LIDAR data, *IEEE T. Geosci. Remote*, 41, 872-882,
783 <https://doi.org/10.1109/TGRS.2003.810682>, 2003.
- 784 Zhang, W., Qi, J., Wan, P., Wang, H., Xie, D., Wang, X., & Yan, G.: An easy-to-use airborne LIDAR data filtering
785 method based on cloth simulation, *Remote Sens.*, 8, 501, <https://doi.org/10.3390/rs8060501>, 2016.